A Sub-100 μm-Range-Resolution Time-of-Flight Range Image Sensor With Three-Tap Lock-In Pixels, Non-Overlapping Gate Clock, and Reference Plane Sampling

A Sub-100μm-range-resolution Time-of-Flight Range Image Sensor with 3-tap Lock-in Pixels, Non-overlapping Gate Clock, and Reference Plane Sampling

Keita Yasutomi, *Member, IEEE*, Yushi Okura, Keiichiro Kagawa, *Member, IEEE*, and Shoji Kawahito, *Fellow, IEEE*

***Abstract*—This study aims to propose a time-of-flight (TOF) range imager with high range resolution in the sub-100 μm range. The range imager employs a TOF measurement technique that uses an impulse photocurrent response and a 3-tap lock-in pixel based on lateral electric field modulation. To reduce the clock skew of the gating clocks, a column-parallel digital delay-locked loop (DLL) with a dual clock tree is implemented with a short calibration time of approximately 42 μs. A non-overlapping gate clock generation included in the skew calibration circuit effectively suppresses photogenerated-charge partitioning for reduced nonlinearity for distance measurements. Reference plane sampling (RPS) is proposed to reduce low-frequency jitter that limits range resolution in the light-pulse trigger. In this technique, a reference pixel array is embedded in the same focal plane of the main pixel array to sample and cancel correlated jitter in the light trigger. The prototype range imager with 192 $\times$ 4 effective pixels is implemented in a 0.11μm CMOS image sensor technology. Using the RPS, a range resolution of 64 $\mu\mathrm{m}_{\mathrm{rms}}$ has been achieved, corresponding to a 430-fs time resolution with a 25-mm range. The range resolution has a large column-to-column deviation due to the jitter induced by the column-parallel gating buffers. In noisy columns, jitter that acts as random telegraph noise (RTN) is observed.**

***Index Terms*—CMOS image sensor, time-of-flight, range imaging, skew calibration, high range resolution, lateral electric field modulator, lock-in pixel, non-overlapping gate clock, DLL-based skew calibration, photogenerated charge partitioning, reference plane sampling.**

I. Introduction

Three-dimensional (3D) scanning systems are widely used in industrial applications, such as dimensional inspection and 3D copying in combination with 3D printers for reverse designs and reverse engineering. The active triangulation method is currently a common technology that offers high precision in contactless 3D scanners [1], [2]. The method, however, requires a long base-line between the camera and the light source to maintain a high range resolution. The base-line limits the head size of the scanners and causes occlusion. On the contrary, time-of-flight (TOF) range image sensors are becoming quite popular in 3D acquisition cameras [3]–[8]. Since the TOF range imaging does not require the base-line, it enables coaxial scanning, occlusionless 3D measurement, and miniaturized 3D scanning systems.

So far, various indirect TOF range imagers have been presented [9]–[18]. They use a pulsed or sinusoidal modulation as light source, and the reflected light is demodulated by a lock-in pixel. Their target applications are mainly gesture or object recognition where resolutions of a few millimeter range are required. However, in 3D scanner applications such as reverse designs and reverse engineering, sub-millimeter or better range resolution is strongly desired.

Frequency modulation (FM) TOF range imaging [19], [20] is one of the important technologies for TOF-based 3D scanners. The optical frequency of the light source is modulated using a tunable laser, and a coherent receiver is used to detect the reflected light and the reference light. Although they offer a high range resolution, the detector with an optical combiner is limited to a single or a few pixels because of its complicated structure and circuitry that requires two-dimensional mechanical scanning. It is difficult to enhance the speed of 3D scanning because of the difficulty associated with realizing high-speed mechanical scanners.

For better range resolutions in the lock-in pixel-based TOF range imaging, the authors have proposed an indirect TOF measuring technique that employs an impulse photocurrent response [21], [22]. It realizes sub-millimeter range resolutions using a short-pulse laser and photocurrent response of the high-speed lock-in pixel based on draining-only modulation (DOM) [23], [24]. Additionally, column-parallel skew calibration is implemented [25], [26], which is essential for simultaneous distance measurements for an entire pixel array in the proposed TOF method. As a result, 3D imaging with a sub-millimeter range resolution of 0.25 mm is demonstrated for 132 $\times$ 120 effective pixels. To improve the range resolution, an increase of signal electrons is generally effective in TOF range imagers. However, the range resolution in the sub-millimeter range is limited by a low-frequency jitter [26] in the light trigger; the increase of signal electrons by an additional accumulation is no longer effective to improve the range resolution.

This study is partly supported by the following: (1) JSPS KAKENHI Grant Numbers JP15H05524, JP18H05240, JP19H02194, (2) the Center of Innovation Program from Japan Science and Technology Agency, JST, (3) Regional-Innovation Ecosystem Program of MEXT, (4) VLSI Design and Education Center (VDEC), the University of Tokyo in collaboration with Cadence Design Systems, Inc., and Mentor Graphics, Inc..

K. Yasutomi, Y. Okura, K. Kagawa, and S.Kawahito are with the Research Institute of Electronics, Shizuoka University, Hamamatsu, Japan (e-mail:{kyasu,yoku, kagawa,kawahito}@idl.rie.shizuoka.ac.jp).

Digital Object Identifier XXXX.

To address these issues, this study presents a high-range resolution TOF range imager with a 3-tap lock-in pixel and non-overlapping gate clock [27]. The 3-tap lock-in pixel based on a lateral electric field modulator (LEFM) [14], [28]–[33] enhances the utilization efficiency of the received light, resulting in high sensitivity. Using the 3-tap lock-in pixel, a fluctuation in the amplitude of the light pulse does not affect the distance calculation, thereby leading to an improvement in the range resolution. To suppress the low-frequency jitter in the light trigger, we have developed a novel technique using reference plane sampling (RPS) with a reference pixel array embedded in the same focal plane of the main pixel array. This technique improves the range resolution significantly. Additionally, range resolution using impulse photocurrent response is theoretically analyzed, and its effectiveness is discussed with experimental results. This modeling aims to clarify the current issues of range resolution toward further improved range resolution. For short calibration times, background skew calibration is implemented using a column-parallel digital delay-locked loop (DLL) and a dual clock tree structure [34]. In this study, the skew calibration is applied to the 3-tap lock-in pixel. In the implementation, a non-overlapping clock generation for gate driving is a key point toward reducing photogenerated-charge partitioning.

The remainder of this paper is organized as follows. Section II describes the indirect TOF measuring technique with impulse photocurrent response and the 3-tap lock-in pixel with LEFM. Section III presents the sensor architecture, pixel circuit, skew calibration circuitry, non-overlapping gate clock generator, and the RPS. Section IV describes the implementation of a prototype chip and the measurement setup. Experimental results of the prototype are discussed in Section V while conclusions are presented in Section VI.

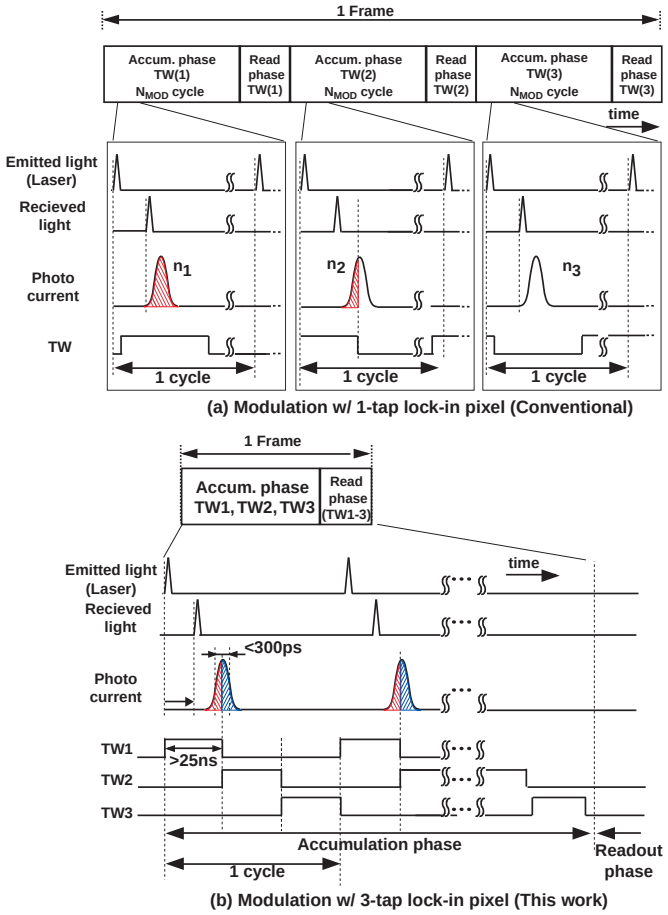

Fig. 1. Indirect TOF measurement technique based on the impulse photocurrent response (a) using a single-tap lock-in pixel and (b) using a 3-tap lock-in pixel.

II. TOF Measurement with 3-tap Lock-in Pixel

A. TOF Measurement with impluse photocurrent response

Figs.1(a) and 1(b) show the TOF measurement methods with the impulse photocurrent response [22] using a single-tap and a 3-tap lock-in pixel, respectively. Instead of using the squared or sinusoidal modulated light source adopted by conventional methods, a short-pulse laser with a pulse width of about a hundred picoseconds is used as the light source to obtain high range resolution. The time-of-flight is calculated from the outputs of the three-phase time-gated signal, where the TW1 and TW2 capture both the light pulse and background light, and the TW3 captures only the background light.

To use the single-tap lock-in pixel, one frame is divided into three sub-frames to capture three time-gated signals with three different-phase time-windows (TWs). In each sub-frame, only a one-phase signal is acquired while the others are drained out. As a result, only one-third of the received light contributes to calculation of the TOF while the rest are discarded. In the 3-tap lock-in pixel, different three-phase signals are simultaneously acquired in a single accumulation cycle. The received light in two TWs (TW1 and TW2) contributes to the TOF calculation, and therefore, the efficiency of light utilization is three times higher than that of the single-tap lock-in pixel. Additionally, a fluctuation in the amplitude of the light pulse does not affect the TOF calculation, thereby contributing toward improving the range resolution.

By using the TOF measurement with the impulse photocurrent response, the measurable range is limited to several centimeters [22], [26]. However, the limited measurable range can be expanded by using a range-shift technique in pulse-based TOF measurements [29], [35]. In the technique, the measurable range is shifted by controlling a trigger of light source, and the measurable range can be expanded by using multiple frames. A proof of this concept, however, is beyond the scope of this paper.

B. 3-tap LEFM with drain

The 3-tap lock-in pixel with a draining structure is implemented by the LEFM [14], [28]–[33] for the high-resolution TOF range imager. Fig. 2 shows its structure [27] and the simulation results of potential distribution. Fig. 3 shows a simulated 3D potential diagram. The device simulations are done by SPECTRA [36]. Four sets of gates (G1, G2, G3, and GD) formed along a pinnned photodiode (PPD) create a lateral electric field in the channel region. The gates are not used for transferring signal electrons through the gate

but are used instead for controlling the channel potential by the fringing electric field from the gates. Since there are no transfer gates in the channel, high-speed charge modulation can be realized, which is similar to 1-tap LEFM or draining-only modulator (DOM) [22], [24], [26]. To avoid unwanted charge accumulation during a readout period, a photogenerated charge under the modulation gates are drained out into Drain2 formed beside the modulation gates. TW1, TW2, and TW3 are assigned to G1, G2, and G3, respectively. The draining gate (GD) is set to high during readout of the three outputs.

The simulation results in Fig. 2 show one-dimentional potential distribution on two directions: A-A' (upper right) and B-B' (lower left), and two-dimentional potential distribution of top view (lower right), where G1 is high (2V) and the other gates are low (-1V). For the A-A' direction, another condition (G2=high, and the other gates=low) is also shown. For the direction of FD1 to FD2 (A-A'), a smooth potential curve is created, leading to high-speed chage modulation. For the B-B' direction, a potential barrier of >85mV is created from the channel to the G1 gate, which is due to the application of the medium voltage (2V) to the G1 gate. Therefore, a signal loss due to leakage from the channel to Drain2 is suppressed to be small. The dashed line in the two-dimentional potential distribution shows an aperture of the LEFM unit. The fill factor of the LEFM unit is 47%. At the lower right of Fig. 2, P1, P2, P3 and the black thick lines shows initial positions and trajectories of electron, respectively. The fringing field of G1 attracts photoelectrons generated in the aperture region to be transferred to FD1.

Fig. 4 shows a simulation result of photocurrent response (G1=high, G2, G3, GD=low). The light pulse is set to a width of 80 ps and photogenerated-currents are monitored at FD1, FD2, FD3, and Drain2. The high-speed photocurrent response is obtained because of the high electric field in the channel (A-A' direction in Fig. 2). The unwanted photocurrents flowing into FD2 and FD3 are negligibly small. The current of Drain2 corresponds to the leakage. The signal loss due to the leakage is only 4% of the photogenerated current monitered at FD1. The Drain2 current is observed mainly when the light is on. When the aperture size is set to 26%, the Drain2 current is reduced to approximately 2%. Therefore, a part of the Drain2 current directly flows from the bulk toward the Drain2 due to the wide aperture setting. The internal quantum efficiency estimated from the simulation result in Fig.4 is 60% at 473 nm in which the signal loss due to the leakage is taken into account. The internal QEs for the other wavelength of 550 nm and 650 nm are simulated to be 58% and 52%, respectively.

C. Distance calculation and its resolution

Assuming a Gaussian function for the photocurrent response, the distance calculated by the time-of-flight, ($D_{\rm tof}$), is derived as follows (See Appendix),

$$D_{\rm tof} = \frac{c}{2}(\sqrt{2\pi}\tau X + T_{ofs}) \quad (1)$$

where c is the speed of light, τ is the intrinsic response time of the photocurrent, T_{ofs} is a time offset that determines the minimum distance of the measurable range, and X is a signal

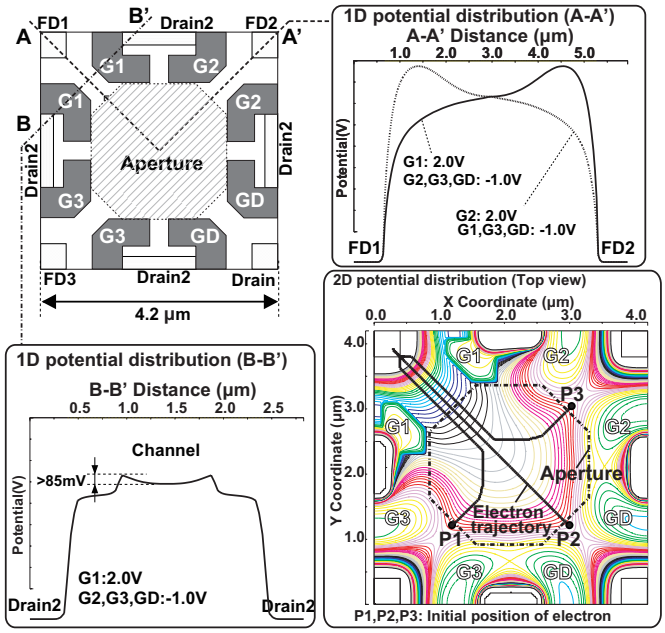

Fig. 2. 3-tap LEFM with drain and simulation results of its potential distribution (Basically, G1=high, G2, G3, GD=low). (Upper right): A-A' potential distribution. (Lower left): B-B' potential distribution. (Lower right): top view of potential distribution. The dashed line in the two-dimentional potential distribution shows an aperture of the LEFM unit.

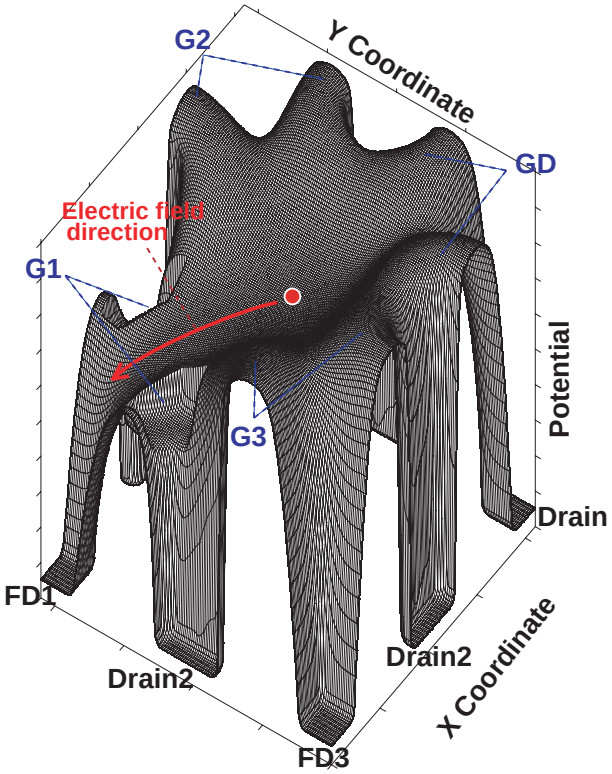

Fig. 3. A simulated 3D potential diagram of 3-tap LEFM when G1=high (2.0 V), and G2, G3, GD=low (-1.0 V).

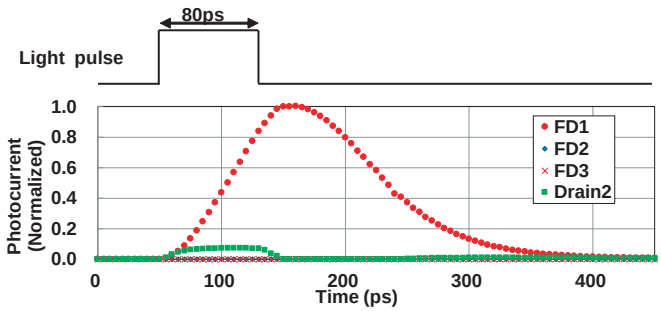

Fig. 4. A transient simulation result on the photocurrent response. A pulsed light with 80 ps width is incident to the aperture area, and the currents at FDs and Drain2 are monitored.

charge ratio defined by

$$X = \frac{N_2 - N_3}{N_1 + N_2 - 2N_3} \quad (2)$$

where N_1, N_2, and N_3 are signal electrons stored in the floating diffusions (FDs) by the gating clocks of G1, G2, and G3, respectively.

Ideally, the measurable range is determined by $\sqrt{2\pi}\tau$ because X takes a value from 0 to 1. Since the calculated distance given by (1) is shifted by changing the T_{ofs}, the T_{ofs} for all pixels must be identical. In reality, however, the T_{ofs} is different from pixel to pixel due to a clock skew in the gating clocks, ΔT_{ofs}. If the skew of a particular pixel is greater than the measurable range, the pixel does not respond to the light pulse, and therefore the time-of-flight is not able to be measured or the measurable range is unacceptably small. As a result, simultaneous TOF measurement for all pixels will fail. In the previous design [26], the measurable range is around 30 mm, corresponding to 200 ps, while the skew of 850 $\mathrm{ps_{p-p}}$ is observed before the skew calibration. For this reason, on-chip skew calibration is indispensable for the proposed TOF method.

Even after the skew calibration, a small amount of skew (around 10 $\mathrm{ps_{rms}}$) still remains [26]. The residual skew causes a variation of distance offsets corresponding to a distance fixed pattern noise (FPN). In addition, many other factors including the variations of RC of the clock lines, variations of the impulse response of the LEFMs and the different path lengths on the optics determines the distance errors (distance FPN, distance non-uniformity, distance non-linearity). The skews due to these factors are also large and dominate the distance errors, but these corresponding skews are not as large as those of column drivers and do not have to be calibrated in on-chip skew-calibration circuits. Therefore, in this paper, the calibration for reducing these distance errors are done by an off-chip correction. This off-chip correction is carried out during the non-linearity calibration for each pixel in the distance measurement described in Section V-B.

The range resolution defined as standard deviation, σ_D, is calculated by error propagation (See the Appendix), resulting in

$$\sigma_D^2 = \frac{D_{MAX}^2}{\overline{N_{sm}}} \left[X(1-X) + \frac{2N_R^2}{\overline{N_{sm}}} \{3X(X-1)+2\} \right] \quad (3)$$

where $D_{MAX}(= \frac{c}{2}\sqrt{2\pi}\tau)$ corresponds to the measurable range, N_R is a dark noise in electrons, and $\overline{N_{sm}}(= \overline{N_1} + \overline{N_2})$ is effective signal electrons used in the range calculation. In (3), the background light component is assumed to be zero, i.e., $\overline{N_3}$ = 0. According to this equation, the range resolution is proportional to the photocurrent response (τ) and inversely proportional to square root of the acquired signal electrons (N_{sm}). The validity of this equation is discussed in Section V-B.

III. Sensor Architecture

A. Comprehensive architecture

Fig. 5 shows the proposed sensor architecture. A part of the pixel array is implemented as reference pixel array used for the RPS. In addition to the pixel array and readout circuits, this sensor has column-parallel skew calibration circuits to reduce column-wise skew. An input clock, $\mathrm{CK_{IN}}$, is distributed to each column via an inverter tree (CK_TREE1) while the gating clocks (G1, G2, G3, and GD) are produced and driven by a clock generator and driver in each column. The propagation of the gating clocks in different paths causes different delays from column to column, corresponding to the skew, ΔT_{ofs}. In particular, the skew generated at the modulation clock driver is dominant because of its large load capacitance of pixel gates. To reduce the column-wise skew, the skew calibration circuit based on digital DLL detects and controls the size of delay at each column so as to minimize the skew.

Folding integration/cyclic ADCs [37] are used in this sensor for readout circuits. Since the pixel pitch of 22.4 μm is four times larger than the ADC pitch of 5.6 μm, each pixel column has four folding integration/cyclic ADCs. The 3-tap outputs from a pixel column are connected to every four ADCs and are converted to digital codes in parallel. One out of every four ADCs is unused and grounded. This is because an intellectual property (IP) core of column ADC with 5.6 μm pitch, and the pixel size is 22.4μm (H) $\times$ 67.2μm (V).

B. Pixel schematic

The pixel schematic and the simplified layout is shown in Fig. 6(a) and 6(b), respectively. The pixel consists of the 3-tap LEFM detectors, reset transistors (RTs), row select transistors (SLs), and source follower transistors (SFs). The FD of each tap is connected to the SF for reading the signal, and a MOS capacitor to enhance its handling capacity. In the schematic, the LEFM gates (G1-G3, and GD) are expressed as virtual switches (SWs) that enable complete charge transfer from the PDs to FDs. The signal change at the FD is read out with an SF amplifier to the column-parallel ADC.

As shown in Fig. 6(b), the LEFM array is a set of 3×5 LEFMs, and it is surrounded by a p+ substrate ring that connected to the ground. The substrate ring isolates LEFM arrays and supplies holes into the LEFM gates and the PPD. Four of the LEFM array (i.e. 60 LEFMs in total) are implemented in the pixel. The LEFM gates and FDs of adjacent LEFMs are unified to maintain the fill factor. Each LEFM unit has a microlens. The fill factor at the pixel level is calculated to 33% where the microlens is not taken into account.

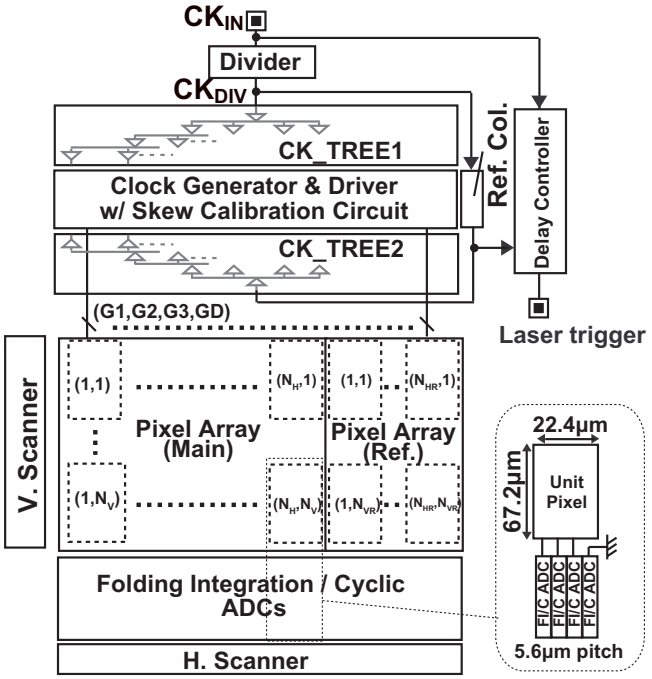

Fig. 5. The proposed sensor architecture with column-parallel skew calibration and a reference pixel array for the RPS.The 3-tap outputs from a pixel column are connected to every four ADCs. One out of every four ADCs is unused and grounded.

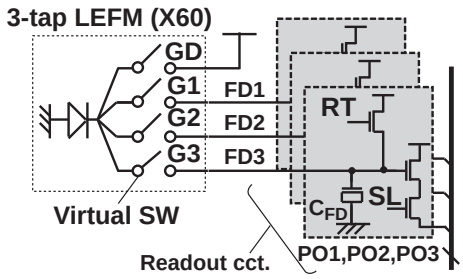

(a) Pixel schematic

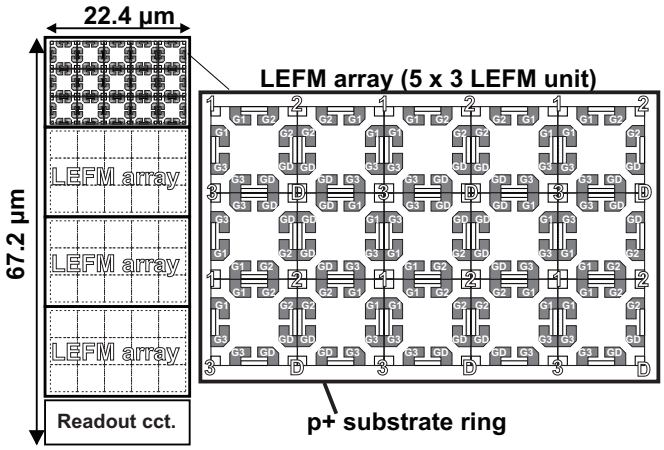

(b) Simplified pixel layout.

Fig. 6. Pixel schematic and simplified layout. The LEFM gates (G1-G3, and GD) are expressed as virtual switches. 60 LEFMs are implemented in the pixel. In the layout, the LEFM gates and FDs of adjacent LEFMs are unified.

As shown in Fig. 1(b), the readout phase begins after the accumulation phase. The SLs are first asserted and the signal levels of each FD are then read out. After the FDs are reset by the RTs, the reset levels are read out. Since these signal and reset levels are serially digitized, the differences between the two levels are taken at the column logic.

C. DLL-based skew calibration

The proposed skew calibration circuit for the 3-tap lock-in pixel is shown in Fig. 7. The phase diagram and timing chart of the skew calibration circuit is shown in Fig. 8. A digital DLL is implemented in a column for an all-electronic skew calibration [34]. To employ the skew calibration technique to 3-tap lock-in pixels, the falling edge of G1 is chosen for the calibration as shown in Fig. 8. This is because the falling edge determines the end of charge accumulation.

The digital DLL comprises a bang-bang phase detector (BPD) and two-stage delay lines with up/down counters (CNTs). A pattern generator (PG) produces the gating clocks: G1(i), G2(i), G3(i), and GD(i) in the i-th column. Apart from the main columns, an additional column is implemented with almost identical design to the main columns. The reference clock, $\mathrm{G1_{REF}}$ produced by the reference column is distributed to the main columns via a clock tree (CK_TREE2). The BPD detects the phase difference between the G1(i) and $\mathrm{G1_{REF}}$, and the result (i.e., up and down signals) are counted by the CNTs only when the enable signals (EN1 and EN2) are asserted. As a result, the delay of each column is adjusted so that the skews between the main columns are minimized. Unlike the hand calibration [26], the self-calibration is completed within a very short time of 42 μs.

In the proposed circuit, two clock-tree outputs (CK_TREE1 and CK_TREE2) are used to distribute the main clock and the reference clock, ($\mathrm{G1_{REF}}$). The mismatch between CK_TREE1 and CK_TREE2 is related to a systematic offset of G1(i) and $\mathrm{G1_{REF}}$ at the BPD inputs, but the mismatch is no problem because it can be compensated by the delay setting in the reference column that can be controlled by external inputs. This additional delay setting for the reference column can be inserted before the first calibration. As described in [34], the design of CK_TREE2 is key toward effective skew calibration, because the skew induced by CK_TREE2 remains after skew calibration. The layout is carefully designed such as symmetry between the columns and the separation of the power line from the other blocks. The circuit design of two-stage delay lines and an SR-latch based BPD is identical to the one proposed in [34].

As shown in Fig. 8, the skew calibration is carried out only once after turning power on, and then the image capture begins. Then, the accumulation and readout phases are repeated. First, the CNTs of the first and second stages are initialized using RT_CNT. Coarse calibration is then performed when EN1 is asserted. Thereafter, EN2 becomes high and fine calibration is carried out. The pulse widths of EN1 and EN2 are set to 256 cycles, corresponding to 20.5 μs when the cycle

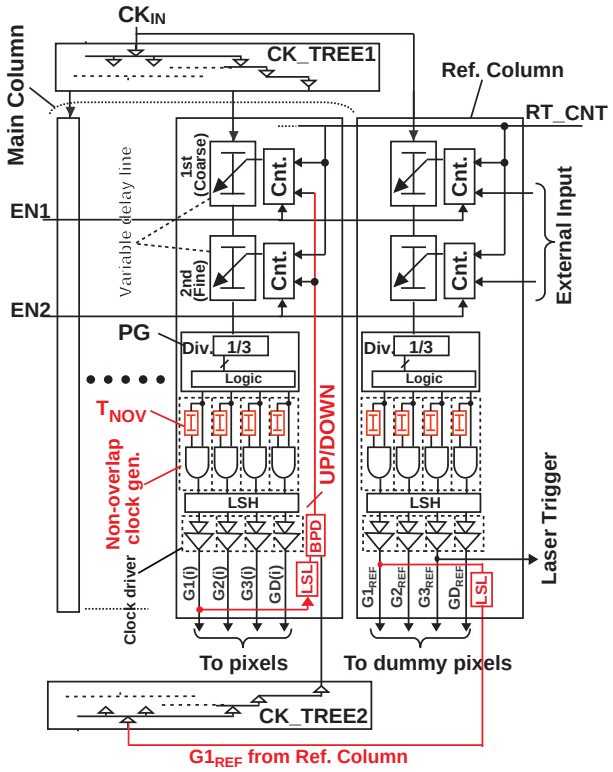

Fig. 7. DLL-based skew calibration circuit with non-overlapping gate clock generation. Level shifters to high and low levels (LSH and LSL, respectively in the figure) are inserted to meet the working voltage range of the gates for the 3-tap LEFM.

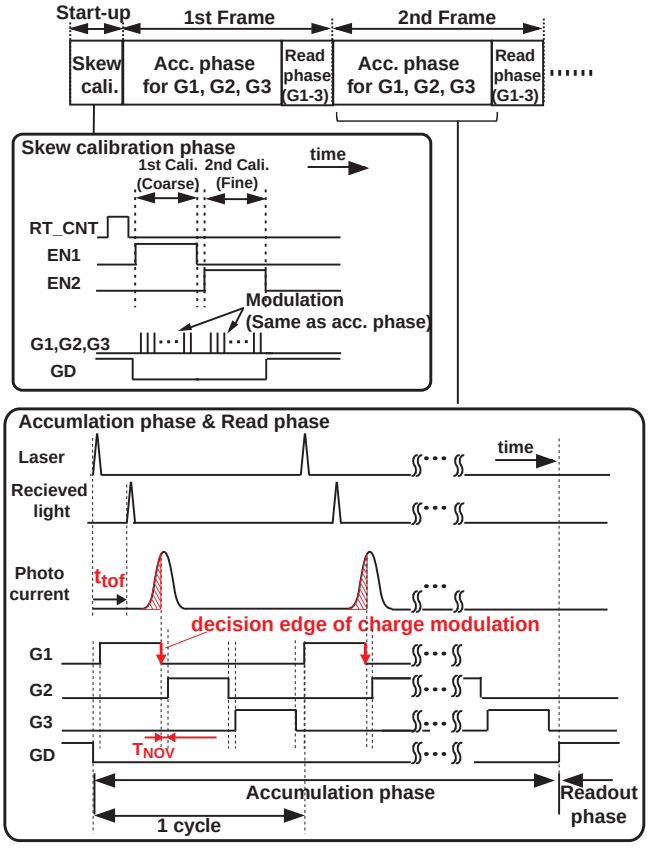

Fig. 8. Phase diagram and timing of the skew calibration circuit. The skew calibration is carried out only once after turning power on, and then the image capture begins; the accumulation and read phases are repeated. For the gate clocks (G1-G3), the non-overlapping time (T_{NOV}) is introduced to avoid the photogenerated-charge partitioning.

time of 80 ns or the repetition frequency of 12.5 MHz is used. The total calibration time including a time margin is 42 μs.

D. Non-overlapping gate clock generation

In the 3-tap lock-in pixel, an overlapping time between the driving pulses of gates, particularly between G1 and G2, causes problems due to photogenerated-charge partitioning. If the driving pulses of G1 and G2 are overlapped, photogenerated-charges at the overlapping time are transferred into both FD1 and FD2, corresponding to the photogenerated-charge partitioning. The photogenerated-charge partitioning leads to large distortions of the modulation characteristics. This issue becomes more critical in short duration light pulses. The overlapping occurs not only from the delay mismatch between the gate drivers but also from the finite settling time of the falling and rising edges of the gates.

To solve the issue, non-overlapping clocks are used to drive the pulses of G1, G2, G3, and GD. Fig. 9(a) shows the schematic of non-overlapping gate clock generator and driver in the column. In this design, the non-overlapping time is contolled by a reference voltage, $V_{R,NOV}$. The non-overlapping gate clock is driven by the column driver in which the fan-out of inverter chain is set to approximately four. The size of final buffer is also shown in Fig. 9(a).

Fig. 9(b) shows simulation results of the transient response of gate clocks: G1 and G2, where the load capacitance of LEFM gates and the metal wiring in the pixel column are taken into account. The potential distributions simulated by SPECTRA at the intersection point of G1 and G2 are also shown in Fig. 9(b). When $V_{R,NOV}$ is set to 1.5V, the gate clocks are overlapped, the resulting intersection point is 1.1V. At the gate voltage, the potential barriers for both G1 and G2 are very small, the photogenerated-charge partitioning occurs. Meanwhile, when $V_{R,NOV}$ is set to 0.8V, the non-overlapping time of 150 ps is observed. At the intersection point of G1 and G2 (-0.7V), the potential barriers of $>$300mV are observed for both G1 and G2. Therefore, the photogenerated electrons are once stored in the PPD. The stored electrons are then transferred to FD2 when G2 becomes high. Since a signal charge per light pulse corresponds to a few electrons even at the saturation level, the barrier height is large enough. Therefore, the signal loss due to the non-overlapping gate clock is expected to be small.

E. Reference Plane Sampling

Ideally, the range resolution given by (3) is determined by the photocurrent response and the photon shot noise. In range resolutions better than sub-millimeter, however, jitters in the gating clock and trigger become dominant. Also, a drift in delay in the trigger circuit, the laser diode (LD) and the LD

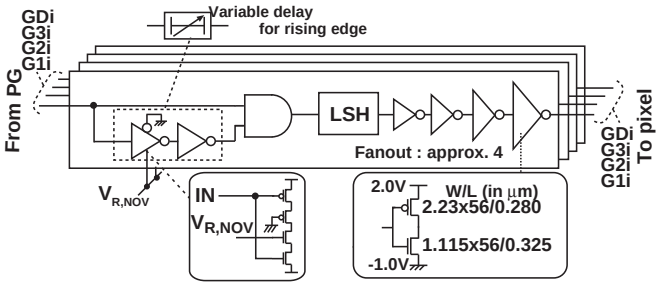

(a) The non-overlapping gate clock generator and driver.

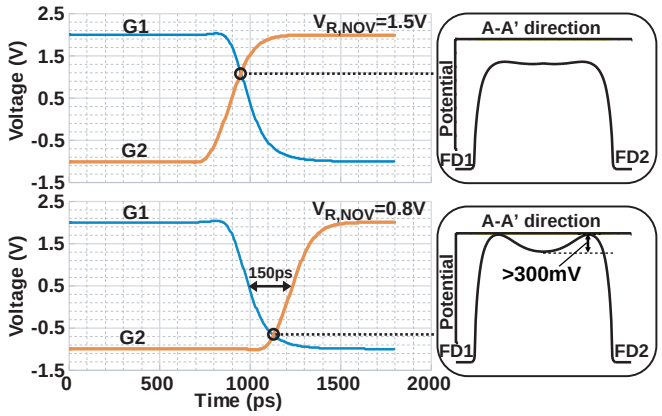

(b) Simulation results of the non-overlapping clock generator and driver. The device simulation results of potential distribution at the intersection point are also shown.

Fig. 9. The non-overlapping gate clock generator and its simulation results.

driver causes a drift in the distance offset. The drift is observed as a low-frequency jitter, and it has a large influence on the measurement on range resolution and 3D capturing of objects. If the overall jitter denoted by $\sigma_{Tjitter}$ as standard deviation is included in (3), it can be rewritten as

$$\sigma_D^2 = \frac{D_{MAX}^2}{N_{sm}}\left[X(1-X)+\frac{2N_R^2}{N_{sm}}\{3X(X-1)+2\}\right] + \left(\frac{c}{2}\right)^2\sigma_{Tjitter}^2. \quad (4)$$

To suppress the jitter, we have developed the RPS using the reference pixel array embedded in the same focal plane of the main TOF pixel array.

Fig. 10 shows the concept of the RPS. The laser light is split into two directions: one for the target and the other is for the reference plane. The reflected light from the reference plane is incident on the reference pixel array. The number of reference pixels is N_{HR}(H)$\times N_{VR}$(V). The reference plane is placed at a fixed known distance within the measurable range. Therefore, the reference pixels always measure the time-of-flight of the known distance.

The measured t_{tof} of the main pixels contains the time-of-flight associated with the distance as well as the jitters caused by the laser module, (σ_{LM}), the delay controller, (σ_{DLC}), the trigger generator, (σ_{TRIG}), and the gating clock, ($\sigma_{COL}(i)$), $i = 1, 2..., N_H$ (See Fig. 10). Additionally, the measured $t_{tof,ref}$ contains σ_{LM}, σ_{DLC}, σ_{TRIG}, and $\sigma_{COL}(i_R)$, $i_R = 1, 2..., N_{HR}$. After the TOF calculations for each pixel, the measured time-of-flights of the reference pixels are averaged to reduce shot noise and jitters at the column of the reference pixels ($\sigma_{COL}(i_R)$). The distance using the RPS at the pixel with coordinates (i,j), $t_{tof,calc}(i,j)$, is calculated by

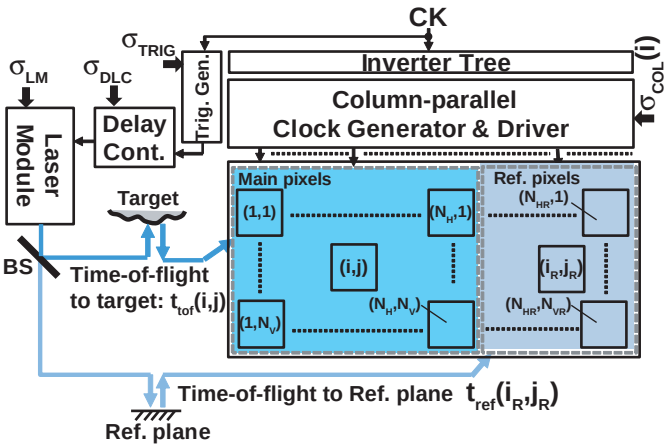

Fig. 10. Concept of the RPS. The laser light is split into the target and the reference plane. The reflected light from the reference plane is incident on the reference pixel array. The reference plane is placed at a fixed known distance within the measurable range. σ_{LM}:the laser module jitter. σ_{DLC}:the delay controller jitter. σ_{TRIG}:the trigger generator jitter. $\sigma_{COL}(i)$:the gating clock jitter.

$$t_{tof,calc}(i,j) = t_{tof}(i,j) - \frac{1}{N_{HR}N_{VR}}\sum_{i_R=1}^{N_{HR}}\sum_{j_R=1}^{N_{HV}} t_{ref}(i_R,j_R) + t_{ref,known} \quad (5)$$

where $t_{tof}(i,j)$ and $t_{ref}(i_R,j_R)$ are the calculated time-of-flights at the main and reference pixels, respectively. N_{HR} and N_{HV} are the number of columns and rows used in the TOF calculation of the reference plane. $t_{ref,known}$ is the known time-of-flight associated with the distance to the reference plane. As a result, the correlated jitters, σ_{LM}, σ_{DLC} and σ_{TRIG} are canceled, while the uncorrelated jitter, σ_{COL}(i) remains.

IV. Implementation and Measurement Setup

A TOF range imager is implemented using a 0.11-μm CMOS image sensor (CIS) technology. The die micrograph is shown in Fig. 11 with a chip size of 9.3 $\times$ 7.3 mm^2. The pixel array consists of 256(H) $\times$ 8(V) pixels in total, where the effective pixels are 192(H) $\times$ 4(V) pixels. In the effective pixels, 32(H)$\times$4(V) pixels are embedded as reference pixels. Apart from the effective pixels, there are several other parameters for testing the pixels.

A short-pulse laser (LDB-160 manufactured by Tama Electric Inc.) is used in the following measurements. The wavelength and pulse width of the laser is 473 nm and $<$ 80 ps, respectively. The laser light is shaped into a line using a line generator lens, and the line width corresponds to four or five pixel rows at a captured image. Since the row-wise

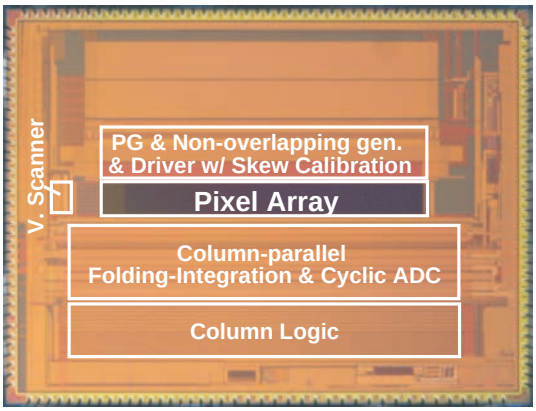

Fig. 11. Chip photograph. The chip is implemented using a 0.11-μm CMOS image sensor (CIS) technology. The chip size is 9.3 $\times$ 7.3 mm^2.

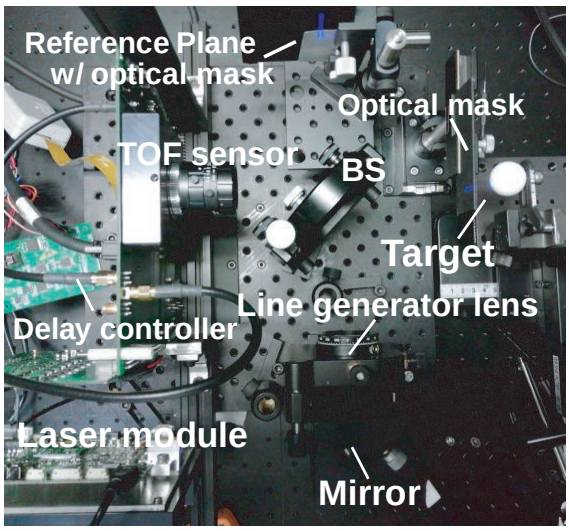

Fig. 12. Measurement setup for the RPS. An emitted light from the laser is split into two directions using a beam splitter (BS). To separate these lights for the target and the reference plane, optical masks (black papers) are used.

illumination is not uniform, only a single row of pixels is discussed in the experimental results described in Section V. The laser-emission trigger is produced by the prototype chip while the delay of the trigger is precisely controlled using a digital delay generator. The repetition frequency of the laser is set to 12.5 MHz, corresponding to the gate pulse width, T_{PW}, of 26.7 ns. The frame rate of the prototype is 24.6 fps when the accumulation time is set to 40 ms, corresponding to a repetition time of 500000.

Fig. 12 shows the measurement setup of the RPS. The laser light is split using a beam splitter (BS), while the lights are emitted to the target and the reference plane. To separate the lights for the target and the reference plane, optical masks (black papers) are used. Although dead pixels or an extra area between the main pixels and the reference pixels are required for the implementation of RPS, the alignment of the optics is not difficult. A stray light in the optics for RPS might be a design challenge to build a practical implementation, which is beyond the scope of this paper. In the following measurements, reference pixels of 32(H)$\times$1(V) are used for the TOF calculation for the reference plane, i.e., $N_{HR} = 32$ and $N_{VR} = 1$ in (5). As is the case for the main pixels, the single row of reference pixels is chosen due to the non-uniformity on the row-wise illumination described above.

V. Experimental Results

A. Suppression of photogenerated-charge partitioning and skew calibration

Figs. 13(a) and (b) show the modulation characteristics of the gated outputs (N_1, N_2, and N_3), X in (2), and its differential value (dX/dt) without and with the non-overlapping gate clock, respectively. In the measurements, the 3-tapped outputs are measured while changing the delay of the laser trigger. For with and without the non-overlapping, $V_{R,NOV}$ is set to 1.5V and 0.8V, respectively. Without the non-overlapping as shown in Fig.9(a), a large distortion is observed due to photogenerated-charge partitioning at the transition from G1 to G2. The distance calculation from the characteristic is difficult. Conversely, with the non-overlapping, the distortion is removed and the transition becomes smooth, thereby reducing the non-linearity error in the distance calculation. The photocurrent response (τ) with the non-overlapping is estimated to 96 ps as shown in Fig. 13(b).

The modulation characteristics are unchanged even when $V_{R,NOV}$ is further reduced from 0.8V because the non-overlapping time is sufficiently large at $V_{R,NOV}$=0.8V. When $V_{R,NOV}$ is set to $<$ 0.7V, the voltage is close to the threshold voltage of nMOS transistors in the delay circuit shown in Fig.9(a), and the non-overlapping generation circuit doesn't work well in some of columns. Therefore, $V_{R,NOV}$ of 0.8V is chosen for the following measurements.

Fig. 14 shows the measured skew distributions with and without the skew calibration. The skew is extracted from modulation characteristics like those shown in Fig.13(b), because the skew is observed as a shift of the transition of G1 and G2. This measurement is a similar way described in [26]. A large skew of 530 ps_{p-p} or 115 ps_{rms} is observed before calibration. The skew includes both random and systematic components that are attributed to the voltage drop in the power supply lines and the device mismatches, respectively. After the skew calibration, the skews are reduced to 54 ps_{p-p} or 10 ps_{rms}. Despite the calibration time of 42 μs being much shorter than that of the hand calibration [26], the residual skew after both calibrations are comparable.

B. Distance measurement

Fig. 15 shows the measured distance, non-linearity error, and range resolution as a function of the distance to a white target with and without the RPS. The range resolution is defined as standard deviation. In the graph, the pixel with coordinates (61,5) is chosen that has a range resolution close to the median value of the main pixel array. In the distance calculation, a fifth-order approximation is used to calibrate non-linearity due to the impulse response of the LEFM. Since this off-chip calibration is carried out for each pixel, the off-

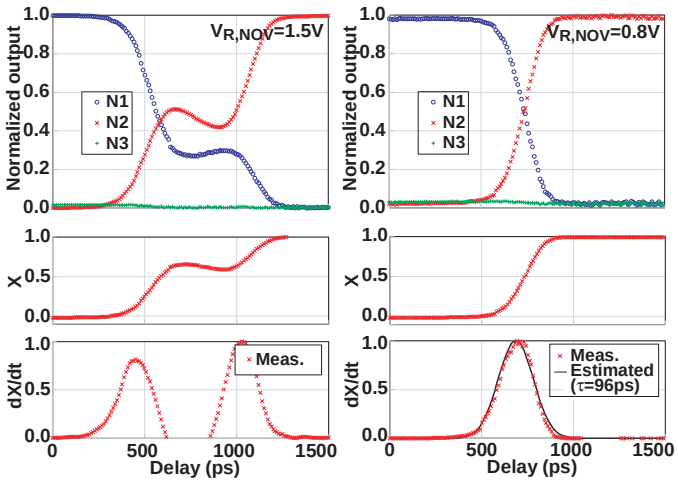

(a) w/o non-overlapping (b) w/ non-overlapping

Fig. 13. Measured modulation characteristics, X and its differential value (dX/dt). (a) without the non-overlapping gate clock ($V_{R,NOV}$=1.5V). (b) with the non-overlapping gate clock ($V_{R,NOV}$=0.8V). For the modulation characteristics, the 3-tapped output is measured while changing the delay of the laser trigger. For the differential value (dX/dt), a moving average is applied. For "with the non-overlapping gate", the estimated photocurrent response of τ=96 (ps) is also shown.

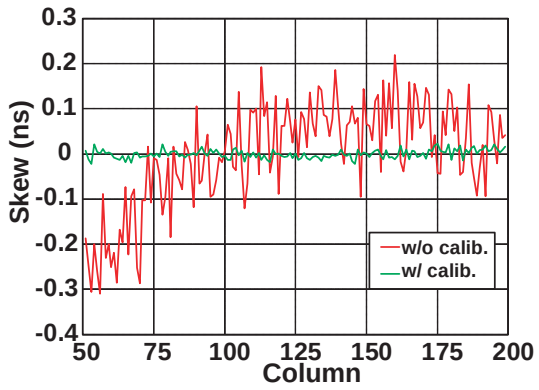

Fig. 14. The measured skew with and without calibration. The skew is extracted from modulation characteristics, because the skew is observed as a shift of the transition of G1 and G2.

chip calibration is effective for variations on the impulse photocurrent responses and modulation clock drivers, and is also effective for a variation of distance offsets (i.e. the distance FPN) due to the residual skew. The different path lengths on the optics of the imaging system are also calibrated. The pixel-level calibration is not special for high accuracy measurement by using TOF range cameras [7]. The non-linearity error and range resolution are calculated using 1000 frames. The measurable range that is defined as the difference between maximum and minimum distance is 25 mm at a non-linearity error of +0.13 mm/-0.23 mm (+0.53%FS/-0.93%FS) using the RPS. Using the RPS, the range resolution is improved from 180 μm to 64 μm, corresponding to a 430-fs time resolution. In the calculation, the median of the range resolution for all the main pixels is taken. In Fig.15, the measured error is slightly improved using the RPS. However, note that the

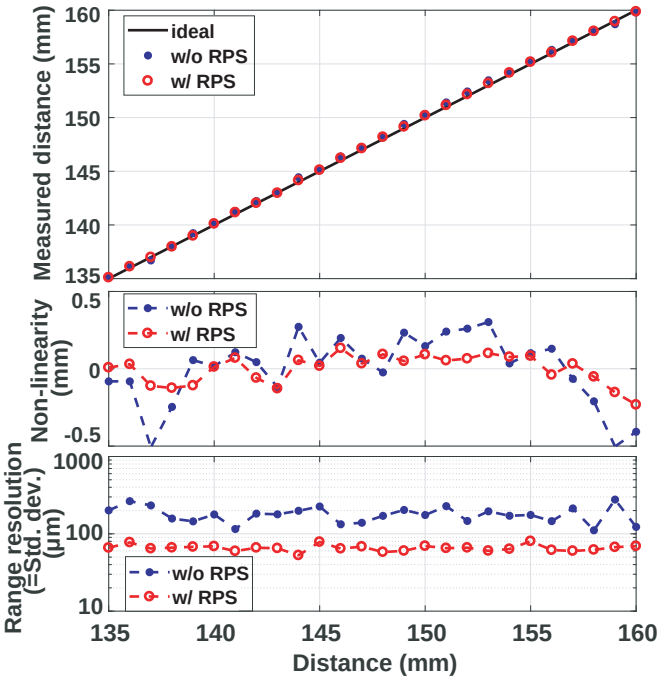

Fig. 15. Measured distance, non-linearity error, and range resolution with and with the RPS @ pixel coordinates (61,5). The white target is used. The non-linearity error is calculated from data averaged by 1000 frames. The range resolution as standard deviation is calculated by 1000 frames.

error should be the same even with the RPS in principle. This improvement is because the measured error is as low as the measurement limit determined by the range resolution. (Note that the range resolution without the RPS is determined by 1/f noise, and therefore averaging using 1000 frames is less effective to reduce the random error due to range resolution.)

Fig. 16 shows the dependence of the range resolution on the signal output. The horizontal axis is the sum of the signal outputs equivalent to N_{sm} in (4). In this measurement, the white target is placed to a fixed distance, and the data are taken while changing the emitted laser power with a variable neutral density (ND) filter. The scatter plot includes 140 pixels in the effective pixels. The calculated resolutions using (4) are also shown in the graph. The intrinsic response (τ), X and the readout noise (N_R) are set to 105 ps, 0.5, and 428 e-$_{rms}$, respectively, as estimated from the measurements. The τ used in here is extracted from the distance measurement, and the value is similar to τ estimated from the modulation characteristic (96 ps). In "Calc. w/o dark noise", $\sigma_{Tjitter}$, and N_R are set to zero. The calculated results with $\sigma_{Tjitter}$ of 1.0 ps and 0.28 ps are also shown as "Calc. w/ dark noise & $\sigma_{Tjitter}$ = 0.28ps" and "Calc. w/ dark noise & $\sigma_{Tjitter}$ = 1.0ps", respectively.

At the low signal output, the measured range resolution is dominated by the dark readout noise. The model of (3) well explains the measured results. As the signal output increases, the range resolution is limited by the jitter component. The estimated jitter component ($\sigma_{Tjitter}$) using the RPS is reduced to 0.28 ps from 1.0 ps, which is the estimated jitter component without using the RPS. The variation of range resolution

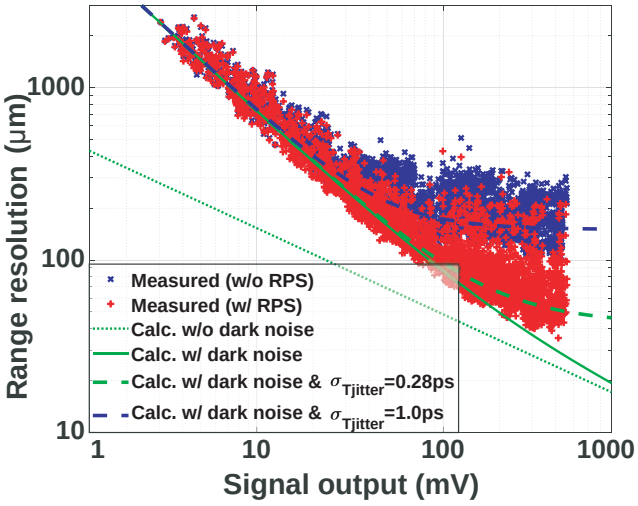

Fig. 16. Dependence of range resolution on signal output. The white target is placed to a fixed distance, and the data are taken while changing the emitted laser power with a variable ND filter. The scatter plot includes 140 pixels in the effective pixels.

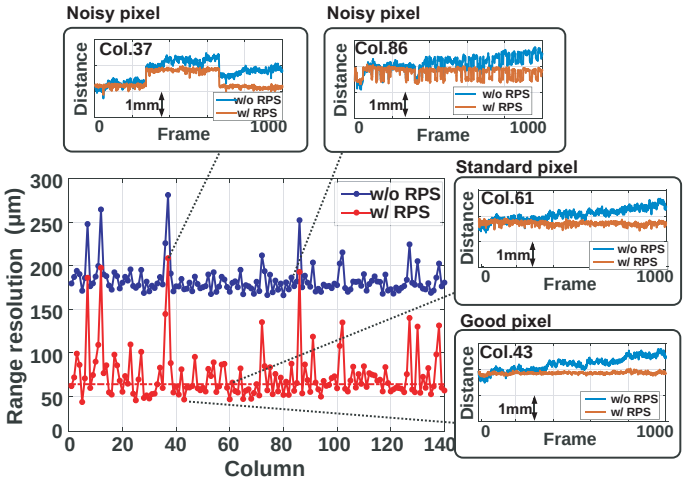

Fig. 17. Dependence of range resolution on the column number and the measured distance as a function of frame number for good (col.43), standard (col.61) and noisy pixels (col.37 and col.86).

shown in Fig. 16 is observed due to different photocurrent responses between pixels, different X values raised from distance FPN, and different amounts of jitters. The residual jitter for the case with the RPS comes from the column gating driver, as described below.

Fig. 17 shows a column-to-column variation of the range resolution. As shown in Fig.17, the range resolution has a large column-to-column deviation. It is also observed that the range resolutions are almost similar between pixels in the same column, though this is not shown in Fig.17. Hence, the jitter induced at the column driver (σ_{COL}(i)) becomes dominant after the RPS. In the noisy columns such as column number 37 and 86, jitter that acts as random telegraph noise (RTN) is observed. One possibility is that the RTN-like jitter is generated at the final stage of the gate driver because its load capacitance is large, leading to the large delay. As shown in Fig. 9(a), the channel length and width of nMOS transistor in the buffer are designed to be 0.325 μm and 64.4μm (=56$\times$1.15 μm), respectively. Despite the transistor size not being small, the RTN-like jitter may be generated. For further improvements in the range resolution, those noises should be reduced. This is beyond the scope of this paper.

Figs. 18 and 19 show sampled point clouds (PCLs) of 3D images generated by the implemented imager with and without the RPS. The object is a ball with a diameter of 20 mm. A one-dimensional mechanical stage is used in the measurement, with the step set to 0.2 mm. Post-processing filters such as the median filter are not applied in these 3D images. As described in Section IV, only a single row of the imager is used, and no binning or averaging between rows is applied in the distance calculation. Therefore, a variation between pixel rows does not appear both in the range resolution and the spatial resolution. In Fig. 18(a), each line is taken without the RPS but with an average of 100 frames. In Fig.18(b), RPS is used but each point is calculated by a single frame. In Fig 18(c), the RPS is used while each line is calculated by an average of 100 frames. In Fig.19, the red dashed line shows an ideal curve of the spherical shape of the ball. Without the RPS, the captured PCL has a large artifact in the stage direction because of the drift or low-frequency jitter. With the RPS, the artifact is effectively suppressed. As a result, an accurate 3D image is obtained even when a single frame is used, as shown in Fig.18(b). The captured PCL is further improved after averaging the data for 100 frames, as shown in Fig.18(c). From Fig.19, the captured PCL with the RPS shows good agreement with the ideal curve for both column and stage axes. From this result, high-accuracy 3D scanning using the prototype has also been demonstrated.

The sensor performance and characteristics are summarized in Table I. The conversion gain of the prototype is calculated to 0.6 μV/e- that is estimated from the parasitic capacitance of FD node. A laser with a wavelength of 473 nm and pulse width of 80 ps is used in the distance measurement. The emitted power of the laser is 360 μW. The median of the range resolution is obtained as 64 μm at a measurable range of 25 mm.

TABLE I
SUMMARY OF THE PERFORMANCE OF THE IMAGER

Parameter		Value
Technology		0.11-μm CIS
Total pixels		257(H) $\times$ 8(V)
Effective pixels		192(H) $\times$ 4(V)
Pixel size		22.4 μm (H) $\times$ 67.2 μm (V)
Fill factor at pixel-level		33%
Conversion gain		0.6 μV/e-
Frame rate (Integration time 40 ms)		24.6 fps
Repetition frequency		12.5 MHz
Emitter	Wavelength	473 nm
	Pulse width	$<$80 ps
	Power	360 μW at the laser output
Measurable range		25 mm at $<\pm$1% Full scale
Range resolution (Median)		64 μm_{rms} (w/ RPS) 180 μm_{rms} (w/o RPS)

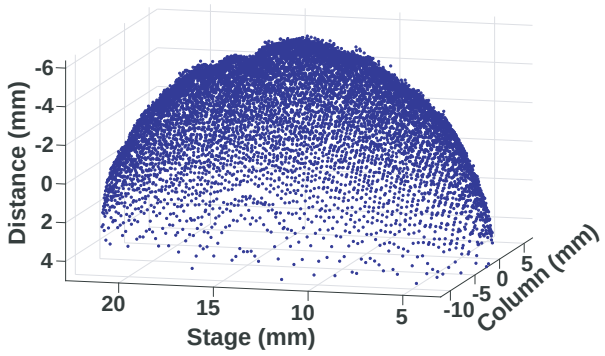

(a) without RPS (100 frame average)

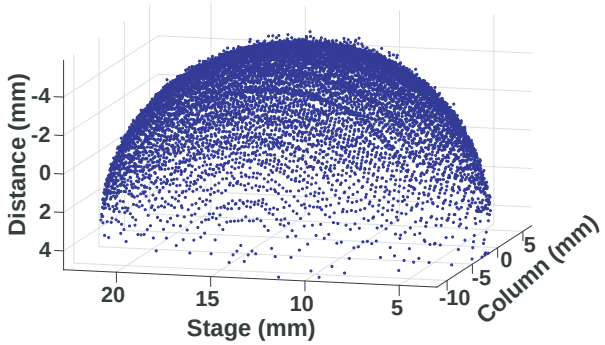

(b) with RPS (single frame)

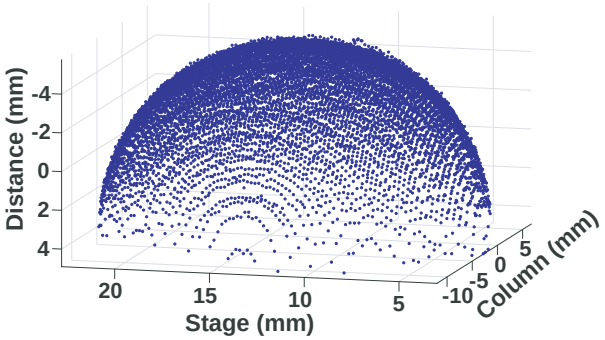

(c) with RPS (100 frame average)

Fig. 18. Point cloud of sampled 3D capture. The target is a ball with a diameter of 20 mm. A one-dimensional mechanical stage with the step of 0.2 mm is used. Post-processing filters are not applied here.

VI. Conclusions

This paper presented a TOF range imager with a 3-tap LEFM, non-overlapping gate clock, and all-electronic skew calibration. The 3-tap LEFM offers three-times higher light utilization efficiency than the single-tap lock-in pixel, and also offers higher capability for suppressing the amplitude drift of the light source. In the skew calibration, the column-parallel digital DLL with dual clock trees reduces the skew between columns. Despite the calibration time of 42 μs being much shorter than that of the hand calibration [26], the residual skews is comparably good. The measured range resolution is improved to 64 μm at a range of 25 mm using the RPS, corresponding to a 430-fs time resolution. Accurate 3D images

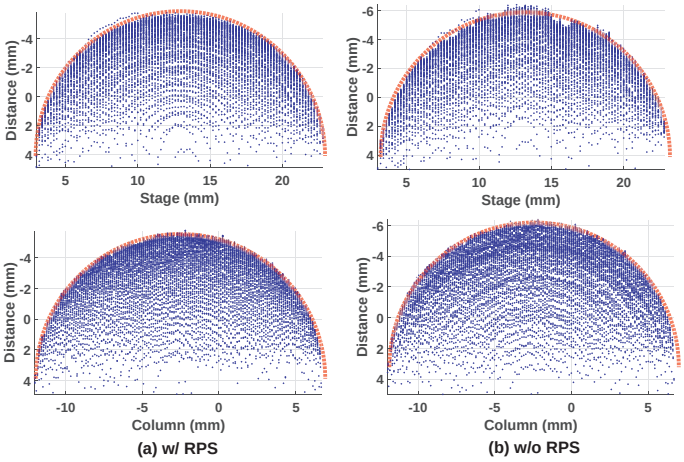

Fig. 19. Point cloud of sampled 3D capture from the scanning stage axis (top) and the column axis (bottom). (a) with RPS. (b) without RPS. The target is a ball with a diameter of 20 mm. he broken red line is an ideal curve.

of a white ball with a 20-mm diameter are successfully acquired by the implemented TOF range imager.

Appendix

Derivation of Time-of-Flight using an impulse photocurrent response with a Gaussian function, and its resolution (Equation (1) and (4))

In the proposed TOF measurement shown in Fig.20, a short light pulse regarded as an impulse is emitted to a target object, and the reflected light generates a photocurrent, I_{ph}, in a photodiode. We assume that the response time associated with the photocurrent is much greater than the light-pulse width. The time of flight, t_{tof}, is then measured by the response time, τ, associated with the photocurrent. Using this TOF measurement technique with a high-speed lock-in pixel, the range resolution is much improved [22]. Here, unlike in [22], the response of the photocurrent is assumed to be a Gaussian function with respect to time in the following discussion. The photocurrent, I_{ph}, is given by

$$I_{ph} = I_M \exp\left\{-\frac{(t-t_{\mathrm{tof,p}})^2}{2\tau^2}\right\} + I_B \tag{6}$$

where I_M and I_B represent a peak photocurrent and a background-light photocurrent, respectively. As shown in Fig.20, three different phases of time windowing are used for the distance calculation while canceling the background light.

For $T_{PW} >> \tau$, we can assume that $T_1 - T_{PW} = -\infty$ and $T_1 + T_{PW} = \infty$. Under this approximation, the accumulated charges, N_1, N_2 and N_3 generated by the time windows, TW1, TW2, and TW3, respectively, are given by

$$\begin{aligned} N_1 &= \frac{1}{q}\int_{T_1-T_{\mathrm{PW}}}^{T_1} I_{ph}dt \approx \frac{1}{q}\int_{-\infty}^{T_1} I_{ph}dt \\ &= \frac{I_M\tau}{q}\sqrt{\frac{\pi}{2}}\left\{1+\mathrm{erf}\left(\frac{T_1-t_{\mathrm{tof},p}}{\sqrt{2}\tau}\right)\right\} + \frac{I_B T_{PW}}{q} \end{aligned} \tag{7}$$

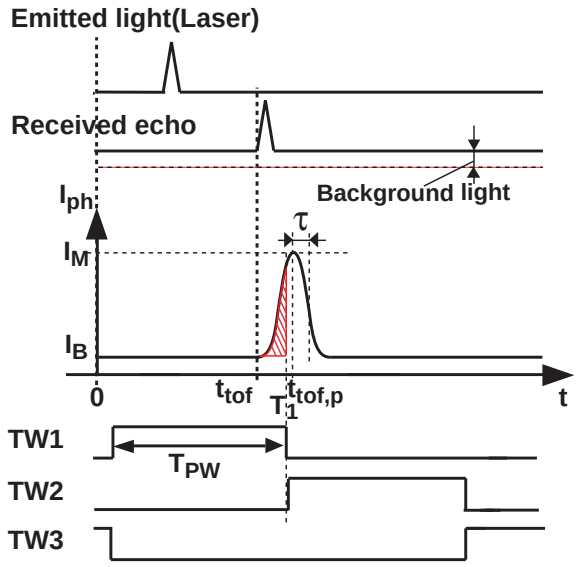

Fig. 20. Indirect TOF Measurement using the photocurrent impulse response with the Gaussian function.

$$N_2 = \frac{1}{q}\int_{T_1}^{T_1+T_{PW}} I_{ph}dt \approx \frac{1}{q}\int_{T_1}^{\infty} I_{ph}dt = \frac{I_M\tau}{q}\sqrt{\frac{\pi}{2}}\left\{1-\mathrm{erf}\left(\frac{T_1-t_{\mathrm{tof},p}}{\sqrt{2}\tau}\right)\right\}+\frac{I_BT_{PW}}{q} \quad (8)$$

$$N_3 = \frac{I_BT_{PW}}{q} \quad (9)$$

where q and T_1 are the elementary charge and an onset of the accumulation of TW1, respectively. The error function, and its first-order approximation are given by

$$\mathrm{erf}(x) \approx \frac{2}{\sqrt{\pi}}x. \quad (10)$$

By solving Eqs. (7)-(8) using first-order approximation to the error function shown in (10), the signal charge ratio, X, can be obtained as

$$X \equiv \frac{N_2-N_3}{N_1+N_2-2N_3} \approx \frac{1}{2}\left\{1+\sqrt{\frac{2}{\pi}}\left(\frac{t_{tof,p}-T_1}{\tau}\right)\right\} \quad (11)$$

where $t_{tof,p}$ is the time from the light emission to the peak of the photocurrent response, as shown in Fig. 20. This equation yields D_{tof} as (1), i.e.,

$$D_{\mathrm{tof}} = \frac{c}{2}(\sqrt{2\pi}\tau X + T_{ofs}). \quad (12)$$

Assuming that the photocurrent response is constant for any target, $T_{ofs}(=T_1-\sqrt{\frac{\pi}{2}}\tau)$ represents an offset that determine the minimum distance for the measurable range.

The range resolution, σ_D, is calculated by error propagation as follows

$$\sigma_D^2 = \left(\frac{c}{2}\right)^2\left\{\left(\frac{\partial t_{tof}}{\partial X}\right)^2\sigma_X^2+\sigma_{Tjitter}^2\right\} \quad (13)$$

where $\sigma_{Tjitter}$ is a jitter of the light trigger and a gating clock like G1 that corresponds to the deviation of T_{ofs}. In general, the jitter in TOF range imagers is much smaller than the first term in (13) and the influence can be negligible. At range resolutions of sub-millimeter or better, however, the jitter becomes dominant.

By solving the partial differentiation, the prefactor of the first term in (13) can be written as follows

$$\frac{c}{2}\frac{\partial t_{tof}}{\partial X} = \frac{c}{2}\sqrt{2\pi}\tau \equiv D_{MAX} \quad (14)$$

where, D_{MAX} corresponds to the measureble range.

By the error propagation theory, σ_X is calculated as

$$\sigma_X^2 = \left(\frac{\partial X}{\partial N_1}\right)^2\sigma_{N_1}^2+\left(\frac{\partial X}{\partial N_2}\right)^2\sigma_{N_2}^2+\left(\frac{\partial X}{\partial N_3}\right)^2\sigma_{N_3}^2. \quad (15)$$

Also, σ_{N_1}, σ_{N_2}, and σ_{N_3} are expressed as

$$\sigma_{N_1}^2 = \overline{N_1}+N_R^2 \quad (16)$$

$$\sigma_{N_2}^2 = \overline{N_2}+N_R^2 \quad (17)$$

$$\sigma_{N_3}^2 = \overline{N_3}+N_R^2 \quad (18)$$

where N_R is dark noise in electron.

In the preceding analysis, background light is taken into account for generality. In our current target, however, the laser power is supposed to be much higher than that of the background light. For this reason, the background light is assumed to be negligible in the following discussions. By substituting Eqs.(15)-(18) into (13), the σ_D^2 is given by

$$\sigma_D^2 = \frac{D_{MAX}^2}{\overline{N_{sm}}}\left[X(1-X)+\frac{2N_R^2}{\overline{N_{sm}}}\{3X(X-1)+2\}\right] + \left(\frac{c}{2}\right)^2\sigma_{Tjitter}^2 \quad (19)$$

where $\overline{N_{sm}}(=\overline{N_1}+\overline{N_2})$ is effective signal electrons in range calculation.

ACKNOWLEDGMENT

The authors thank DB HiTek for chip fabrication. The authors gratefully acknowledge M. Tamaya, Pulstec Industrial Co., Ltd. for helpful discussion in 3D measurement.

REFERENCES

[1] GOM GmbH, ATOS CompactScan, [Online]. Available: https://www.gom.com/metrology-systems/atos/atos-compact-scan.html. [Accessed Dec.10, 2018].

[2] Pulstec Industrial Co., Ltd., TDS-L 3D scanner series, [Online]. Available: https://www.pulstec.co.jp/en/pr/opt/pr_o02.html. [Accessed Dec.10, 2018].

[3] Microsoft, Kinect in Xbox One, [Online]. https://www.xbox.com/en-US/. [Accessed Dec.10, 2018].

[4] Infineon Technologies AG, "Smallest 3D camera worldwide brings Augmented Reality to a smartphone," 2016. [Online], Available: https://www.infineon.com/cms/en/about-infineon/press/press-releases/2016/INFXX201606-064.html. [Accessed Dec.10, 2018].

[5] pmdtechnologies ag, "pmdtechnologies coming strong - New Tango phone from Asus using pmd 's Time-of-Flight technology enables smartphone Augmented & Virtual Reality," Jan. 2017. [Online], Available: https://pmdtec.com/html/pdf/press_release/PR_20170501_pmdinsideASUSphone.pdf. [Accessed Dec.10, 2018].

[6] Radu Horaud, Miles Hansard, Georgios Evangelidis, Clement Menier, "An Overview of Depth Cameras and Range Scanners Based on Time-of-Flight Technologies," *Machine Vision and Applications Journal*, vol.27, no.7, pp.1005-1020, 2016.
[7] H. Sarbolandi, M. Plank, and A. Kolb, "Pulse Based Time-of-Flight Range Sensing," *Sensors*, Vol. 18, No. 6, p. 1679, May. 2018.
[8] P. Fursattel, S. Placht, M. Balda, C. Schaller, H. Hofmann, A. Maier, C. Riess,, " A Comparative Error Analysis of Current Time-of-Flight Sensors, " IEEE Trans. Computational Imaging Vol.2, No.1, Mar. 2016.
[9] T. Spirig, P. Seitz, O. Vietze, and F. Heitger, "The lock-in CCD-two-dimensional synchronous detection of light," *IEEE J. Quantum Electron.*, vol. 31, no. 9, pp. 1705-1708, 1995.
[10] R. Lange and P. Seitz, "Solid-state time-of-flight range camera," *IEEE J. Quantum Electron.*, vol. 37, no. 3, pp. 390-397, Mar. 2001.
[11] S. Kawahito, I.A. Halin, T. Ushinaga, T. Sawada *et al.*, A CMOS time-of-flight range image sensor with gates-onfield-oxide structure," IEEE Sensors J., vol. 7, no. 12, pp. 1578-1586, Dec. 2007.
[12] D. Stoppa, N. Massari, L. Pancheri, M. Malfatti, M. Perenzoni, and L. Gonzo, "A Range Image Sensor Based on 10-μm Lock-In Pixels in 0.18-μm CMOS Imaging Technology," *IEEE J. Solid-State Circuits*, Vol. 46, No. 1, pp. 248-258, Dec. 2011.
[13] S-J. Kim, D.K. Kim, B. Kang K. Lee, "A CMOS Image Sensor Based on Unified Pixel Architecture With Time-Division Multiplexing Scheme for Color and Depth Image Acquisition," *IEEE J. Solid-State Circuits*, Vol. 47, No. 11, pp. 2834-2845, Nov. 2012.
[14] S.-M. Han, T. Takasawa, K. Yasutomi, S. Aoyama, K. Kagawa, and S. Kawahito, " A Time-of-Flight Range Image Sensor with Background Cancelling Lock-in Pixels Based on Lateral Electric Field Charge Modulation, " *IEEE J. Electron Devices Soc.*, Vol. 3, No.3, pp.267-275, May. 2015.
[15] C. S. Banji, P. O 'Connor, T. Elkhatib, S. Mehta, B. Thompson, L. A. Prather, D. Snow, O. C. Akkaya, A. Daniel, A. D. Payne, T. Perry, M. Fenton, V-H. Chan, "A 0.13 μm CMOS System-on-Chip for a 512 $\times$ 424 Time-of-Flight Image Sensor With Multi-Frequency Photo-Demodulation up to 130 MHz and 2 GS/s ADC," *IEEE J. Solid-State Circuits*, Vol. 46, No. 1, pp. 248-258, Jan. 2015.
[16] E. Tadmor, D. Cohen, G. Yahav, G. Tennenholtz, G. Lehana, A. Lahav, A. Birman, A. Fenigstein, A. Fish, " Development of a ToF Pixel With VOD Shutter Mechanism, High IR QE, Four Storage, and CDS, " *IEEE Electron Devices*, Vol.63, No.7, pp. 2892-2896, Jul. 2016.
[17] Y. Kato, T. Sano, Y. Moriyama, S. Maeda, T. Yamazaki, A. Nose, K. Shiina, Y. Yasu, W. v. d. Tempel, A. Ercan, Y. Ebiko, D. V. Nieuwenhove, and S. Sukegawa, "320 $\times$ 240 Back-Illuminated 10-μm CAPD Pixels for High-Speed Modulation Time-of-Flight CMOS Image Sensor," *IEEE J. Solid-State Circuits*, Vol. 53, No. 4, pp. 1071-1078, Apr. 2018.
[18] C. S. Bamji, S. Mehta, B. Thompson, T. Elkhatib, S. Wurster, O. Akkaya, A. Payne, J. Godbaz, M. Fenton, V. Rajasekaran, L. Prather, S. Nagaraja, V. Mogallapu, D. Snow, R. McCauley, M. Mukadam, I. Agi, S. McCarthy, Z. Xu, T. Perry, W. Qian, V.-H. Chan, P. Adepu, G. Ali, M. Ahmed, A. Mukherjee, S. Nayak, D. Gampell, S. Acharya, L. Kordus, P. O'Connor, "1Mpixl 65nm BSI 320MHz Demodlated ToF Image Sensor with 3.5 μ m Global Shutter Pixels and Analog Binning," *Dig. Tech. Papers, IEEE Int. Solid-State Circuits Conf. (ISSCC)*, pp. 94-95, Feb, 2018.
[19] F. Aflaouni, B. Abiri, A. Rekhi, A. Hajimiri, "Nanophotonic coherent imager," *OPTICS EXPRESS*, 23(4), pp.5117-5125 (2015).
[20] B.Behroozpour, P.A.M.Sandborn, N.Quack, T.-J.Seok, Y.Matsui, M.C.Wu, and B.E.Boser, " Electronic-Photonic Integrated Circuit for 3D Microimaging, " *IEEE J. Solid-State Circuits*, vol. 52, no. 1, pp. 161-172, 2017.
[21] K. Yasutomi, T. Usui, M. Kodama, S. Han, T. Takasawa, K. Kagawa, and S. Kawahito, "A time-of-flight image sensor with sub-mm resolution using draining only modulation pixels," *in Proc. 2013 Intl. Image Sensor Workshop*, pp.357-360, 2011.
[22] K. Yasutomi, T. Usui, S. Han, T. Takasawa, K. Kagawa, and S. Kawahito, "An indirect time-of-flight measurement technique with impulse photocurrent response for sub-millimeter range resolved imaging," *OPTICS EXPRESS*, 22(16), pp.18904-18913 (2014).
[23] S. Kawahito, Z. Li, K. Yasutomi, "A CMOS image sensor with draining only demodulation pixels for time-resolved imaging," *in Proc. 2011 Intl. Image Sensor Workshop*, pp.185-188, Hakodate, Jun. 2011.
[24] Z. Li, S. Kawahito, K. Yasutomi, K. Kagawa, J. Ukon, M. Hashimoto, and H. Niioka, "A time-resolved CMOS image sensor with draining-only modulation pixels for fluorescence lifetime imaging," *IEEE Trans. Electron Devices*, Vol.59, No.10, pp.2715-2722, Oct. 2012.
[25] K. Yasutomi, T. Usui, S. Han, T. Takasawa, K. Kagawa, and S. Kawahito, "A 0.3mm-resolution time-of-flight CMOS range imager with column-gating clock-skew calibration," *Dig. Tech. Papers, IEEE Int. Solid-State Circuits Conf. (ISSCC)*, pp. 132-133, Feb, 2014.
[26] K. Yasutomi, T. Usui, S-M. Han, T. Takasawa, K. Kagawa, S. Kawahito, "A Submillimeter Range Resolution Time-of-Flight Range Imager with Column-wise Skew Calibration," *IEEE Trans. Electron Devices*, Vol.63, No.1, pp.182-188, Jan. 2016.
[27] K. Yasutomi, Y. Morikawa, S. Imanishi, T. Takasawa, K. Kagawa, S. Kawahito, "A high-resolution time-of-flight range image sensor with a 3-tap lateral electric field charge modulator," Proc. of 2017 *International Image Sensor Workshop*, R24, pp.254-257, Jun. 2017.
[28] S. Kawahito, G. Beak, Z. Li, S.-M. Han, M.-W. Seo, K. Yasutomi, and K. Kagawa, " CMOS Lock-in Pixel Image Sensors with Lateral Eelectric Field Cotrol for Time-Resolved Imaging, " *in Proc. 2013 Int. Image Sensor Workshop*, pp. 361-364, Jun. 2013.
[29] T. Kasugai, S-M.Han, H. Trang, T. Takasawa, S. Aoyama, K. Yasutomi, K. Kagawa, S. Kawahito, "A Time-of-Flight CMOS Range Image Sensor Using 4-Tap Output Pixels with Lateral-Electric-Field Control " *in Proc. of IS&T International Symposium on Electronic Imaging 2016*, pp.IMSE-048.1-6, 2016.
[30] Y. Morikawa, K. Yasutomi, S. Imanishi, T. Takasawa, K. Kagawa, N. Teranishi, and S. Kawahito, "A Lateral Electric Field charge Modulator with Bipolar-gates for Time-resolved Imaging" *in Proc. of IS&T International Symposium on Electronic Imaging 2017*, pp.64-67, 2017.
[31] Z. Li, M. W. Seo, K. Kagawa, K. Yasutomi, and S. Kawahito, " CMOS image sensor with lateral electric field modulation pixels for fluorescence lifetime imaging with sub-nanosecond time response, " *Japanese Journal of Applied Physics*, vol. 55, no. 04EM06, pp. 1-7, Mar. 2016.
[32] M.-W. Seo, K. Kagawa, K. Yasutomi, Y. Kawata, N. Teranishi, Z. Li, I.A. Halin, S. Kawahito, "A 10 ps Time-Resolution CMOS Image Sensor With Two-Tap True-CDS Lock-In Pixels for Fluorescence Lifetime Imaging," *IEEE J. Solid State Circuits*, vol.51, No.1, pp.141-154 , 2016.
[33] M.-W. Seo, Y. Shirakawa, Y. Kawata, K. Kagawa, K. Yasutomi, S. Kawahito, "A Time-Resolved Four-Tap Lock-In Pixel CMOS Image Sensor for Real-Time Fluorescence Lifetime Imaging Microscopy," *IEEE J. Solid State Circuits*, vol.53, No.8, pp.2319-2330, 2018.
[34] L. Miao, K. Yasutomi, S. Imanishi, S. Kawahito, "A Column-Parallel Clock Skew Self-Calibration Circuit for Time-Resolved CMOS Image Sensors," *IEICE Electronics Express*, Vol.12, No.24, pp. 20150911, Dec. 2015.
[35] T. Sawada, K. Ito, M. Nakayama, S. Kawahito, "TOF range image sensor using a range-shift technique," *in Proc. of IEEE SENSORS 2008* pp.1390-1393, Oct.2008.
[36] H. Mutoh, "3-D Optical and Electrical Simulation for CMOS Image Sensors," *IEEE Trans. Electron Devices*, Vol.50, No. 1, pp.19-25, May 2003.
[37] M.-W. Seo, S.-H. Suh, T. Iida, T. Takasawa, K. Isobe, T. Watanabe, S. Itoh, K. Yasutomi, and S. Kawahito, "A Low-Noise High Intrascene Dynamic Range CMOS Image Sensor With a 13 to 19b Variable-Resolution Column-Parallel Folding-Integration/Cyclic ADC," *IEEE J. Solid-State Circuits*, Vol. 47, No. 1, pp. 272-283, Jan. 2012.

Keita Yasutomi (S'08-M'11) received the Ph.D. degree from Shizuoka University, Hamamatsu, Japan, in 2011. Since 2012, he has been an Assistant Professor with the Research Institute of Electronics, Shizuoka University. He is a member of the Institute of Image Information and Television Engineers and a member of Institute of Electronics, Information, and Communication Engineers. His research interests include time-of-flight range imagers, time-resolved CMOS image sensors and low-noise imagers.

Yushi Okura received the B.E. degree from Shizuoka University, Hamamatsu, Japan, in 2018. He is currently pursuing the M.E. degree at Shizuoka University.

Keiichiro Kagawa (M'10) received the Ph.D. degree in engineering from Osaka University, Osaka, Japan, in 2001. In 2001, he joined Graduate School of Materials Science, Nara Institute of Science and Technology as an Assistant Professor. In 2007, he joined Graduate School of Information Science, Osaka University as an Associate Professor. Since 2011, he has been an Associate Professor with Shizuoka University, Hamamatsu, Japan. His research interests cover high-performance CMOS image sensors, imaging systems, and biomedical applications.

Shoji Kawahito (S'86-M'88-SM'00-F'09) received the Ph.D. degree from Tohoku University, Sendai, Japan, in 1988. Since 1999, he has been a Professor with the Research Institute of Electronics, Shizuoka University. Since 2006, he has been the CTO of Brookman Technology Inc., Hamamatsu, Japan, a University spin-off company for CMOS imager developments. He has authored over 300 papers in peer-reviewed journals and international conference-proceedings. His current research interests include CMOS imaging devices, sensor interface circuits, and mixed analog/digital circuits designs.

Dr. Kawahito is a fellow of the Institute of Image Information and Television Engineers and a member of Institute of Electronics, Information, and Communication Engineers and SPIE. He received several awards, including the Outstanding Paper Award at the 1987 IEEE International Symposium on Multiple-Valued Logic, the Special Feature Award in the LSI Design Contest at the 1998 Asia and South Pacific Design Automation Conference, the Beatrice Winner Award for Editorial Excellence at the 2005 IEEE International Solid-State Circuits Conference, the IEICE Electronics Society Award in 2010, the Takayanagi Memorial Award in 2010, and the Walter Kosonocky Award in 2013. He served as a Technical Program Committee Member of the International Solid-State Circuits Conference from 2009 to 2012 and the Program Committee Chair of the 2011 International Image Sensor Workshop. He is the Chair of the Solid-State Circuits Society Japan Chapter from 2013 to 2014.